Geometry-Engineered Copper Redox Interfaces Drive Highly Selective CO_2 Reduction to C_2 Products

Nitul Kalita,† Jagnyesh K. Satpathy,† Ankit Kumar Singh,† Upasana Nath,† Manabendra Sarma,† Chivukula V. Sastri† and Mohammad Qureshi*†*

†Department of Chemistry, Indian Institute of Technology Guwahati, 781039, Assam, India

1. Synthesis of heterogeneous catalyst ($Cu_{1.5}Mn_{1.5}O_4$)

Commercial carbon paper (0.2 × 0.5 cm^2) was initially cleaned to eliminate surface impurities. The pretreated substrate was then immersed in a homogeneous aqueous solution containing 0.5 M manganese(II) acetate, 0.2 M copper(II) acetate, and 0.5 M urea (total volume: 30 mL). This precursor solution was transferred into a 50 mL Teflon-lined stainless-steel autoclave and subjected to hydrothermal treatment at 160 °C for 20 h to promote the in situ growth of a $CuMn(OH)_x$ intermediate layer on the substrate. Upon completion, the resulting film was thoroughly rinsed with ethanol and deionized water, followed by vacuum drying at 60 °C. Final crystallization was achieved by calcination in air at 900 °C for 2 h using a ramp rate of 5 °C min^{-1}, yielding the phase-pure $Cu_{1.5}Mn_{1.5}O_4$ catalyst.

2. Synthesis of homogeneous catalyst

2.1 Synthesis of flexible ligand (L1)

Ligand $L1_{Flex}$ was synthesized following a modified procedure based on previously reported methods.[1-3] Briefly, dimethyl acetonedicarboxylate (1.0 equiv) was dissolved in 20 mL of methanol and cooled to 273 K. A premixed solution of aqueous formaldehyde (2.0 equiv) and 2-picolylamine (1.0 equiv) was added dropwise under stirring. After complete addition, the reaction mixture was stirred overnight at 273 K. The resulting white precipitate was collected by filtration, washed with cold ethanol, and dried under vacuum. The product, obtained in >97% purity, was used directly in the subsequent step without further purification.

For the second condensation step, the above white solid (1.0 equiv) was suspended in 200 mL of ethanol. Aqueous formaldehyde (37%, 2.1 equiv) and 2-picolylamine (1.0 equiv) were added dropwise to the suspension under continuous stirring. The reaction mixture was refluxed for 4 h, yielding a brown solution upon completion. The solvent

was then concentrated, and the solution was stored at 258 K. After several days, a white crystalline solid formed, which was collected and recrystallized from acetonitrile to afford the final ligand.

2.2 Synthesis of rigid ligand (L2)

The ligand $L2_{Rigid}$ was synthesized following a modified literature procedure.[4] Dimethyl acetonedicarboxylate (4.80 mL, 33.33 mmol) was dissolved in 20 mL of methanol and cooled to −10 °C. A premixed solution of pyridine-2-carboxaldehyde (6.37 mL, 66.66 mmol) and methylamine (33.33 mmol) was added dropwise under continuous stirring. Upon complete addition, the reaction mixture was allowed to warm to ambient temperature and stirred overnight. A white precipitate of the piperidone intermediate formed, which was collected by filtration, washed thoroughly with cold ethanol, and dried under reduced pressure. The product was obtained in ~84% yield and used directly in the subsequent step without further purification.

To synthesize the bispidine ligand $L2_{Rigid}$, the isolated piperidone (12.70 g, 33.10 mmol) was suspended in 200 mL of ethanol. Aqueous formaldehyde (37%, 6.50 mL, 79.40 mmol) and methylamine (39.70 mmol) were added dropwise under stirring. The mixture was refluxed for 4 h, yielding a clear brown solution. After cooling, the reaction mixture was concentrated to half of its original volume and stored at −20 °C. After several days, white crystalline solids were obtained and collected by filtration.

3. Synthesis of Cu Complexes (Cu^{L1}_{Flex} Cu^{L2}_{Rigid})

Ligands $L1_{Flex}$ and $L2_{Rigid}$ were individually reacted with Cu (II)$(ACN)_2(OTf)_2$ in acetonitrile under ambient conditions. Each reaction mixture was stirred overnight and subsequently filtered through PTFE membranes. The resulting filtrates were layered with diethyl ether and stored at 233 K to facilitate crystallization. Single crystals suitable for X-ray diffraction of the complex $[Cu^{L1}_{Flex}]$ and $[Cu^{L2}_{Rigid}]$ were obtained by slow vapor diffusion into the acetonitrile solution.

4. ^{1}H and ^{13}C NMR data:

Presented below are the ^{1}H and ^{13}C NMR spectra of $L1_{Flex}$ and $L2_{Rigid}$, confirming the successful synthesis of these ligands.

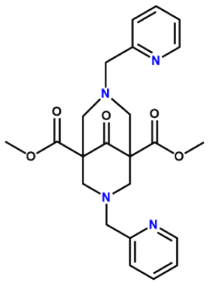

$L1_{Flex}$

(a)

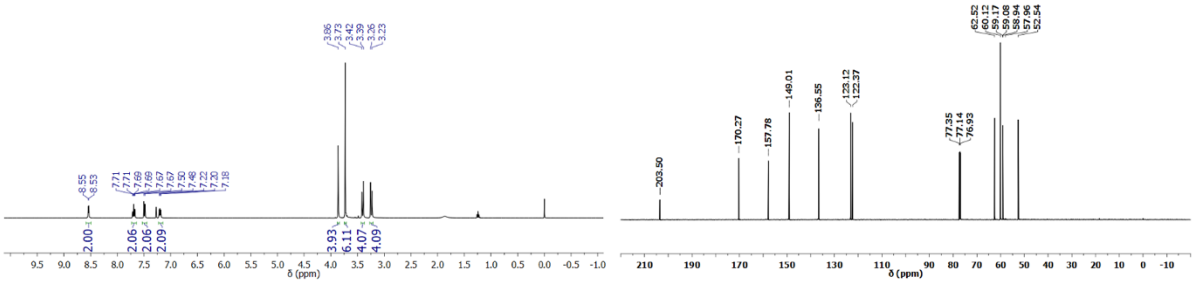

Figure S1. ^{1}H (a) and ^{13}C (b) NMR spectra of the $L1_{Flex}$ ligand

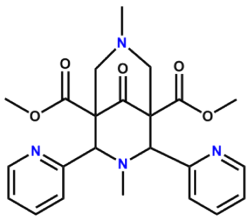

$L2_{Rigid}$

(a)

(b)

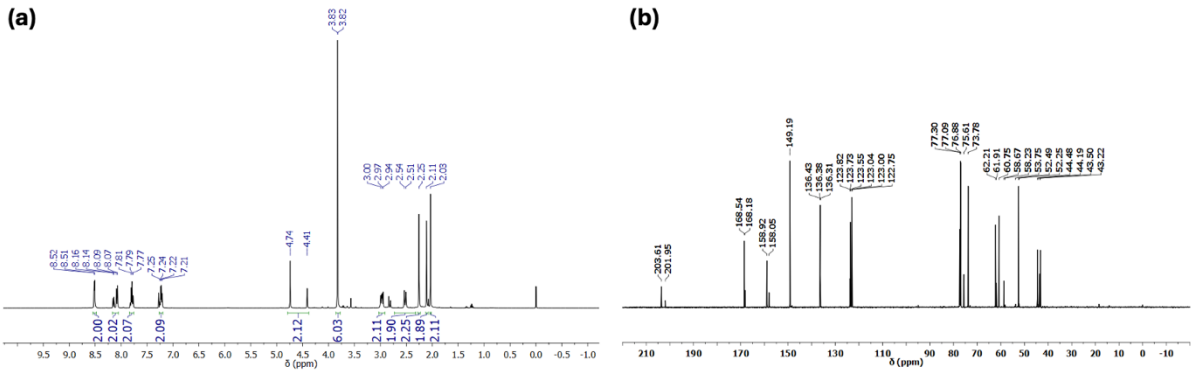

Figure S2. ^{1}H (a) and ^{13}C (b) NMR spectra of the $L2_{Rigid}$ ligand

5. UV-Vis spectroscopy:

The UV–vis spectra of the copper (II) complexes display characteristic ligand-to-metal charge transfer bands. Noticeable variations in both λ_{max} and molar extinction coefficients (ε) are observed, which highlight the influence of the distinct coordination environments on the electronic structures of the complexes.

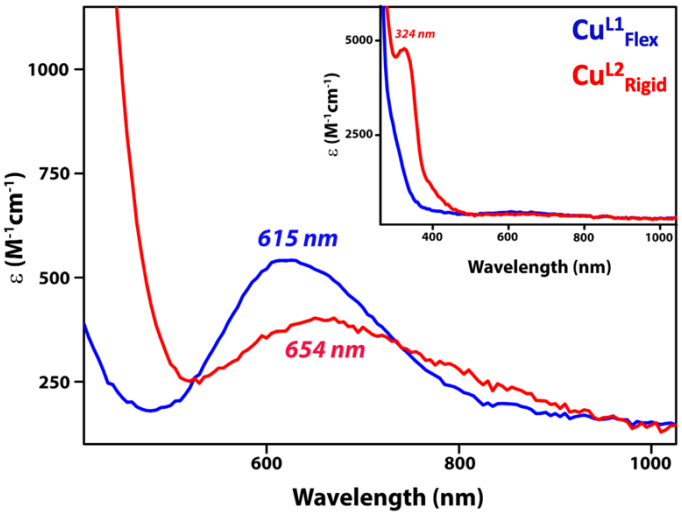

Figure S3. UV–vis spectra of the copper (II) complexes showing ligand-to-metal charge transfer bands.

6. Electron paramagnetic resonance (EPR) spectroscopy:

The EPR spectra of [Cu^{L1}_{Flex}] and [Cu^{L2}_{Rigid}] exhibit isotropic signals with g values of 2.11 and 2.13, respectively, consistent with Cu (II) centers in slightly different coordination environments. These data support the presence of paramagnetic Cu (II) species in both complexes.

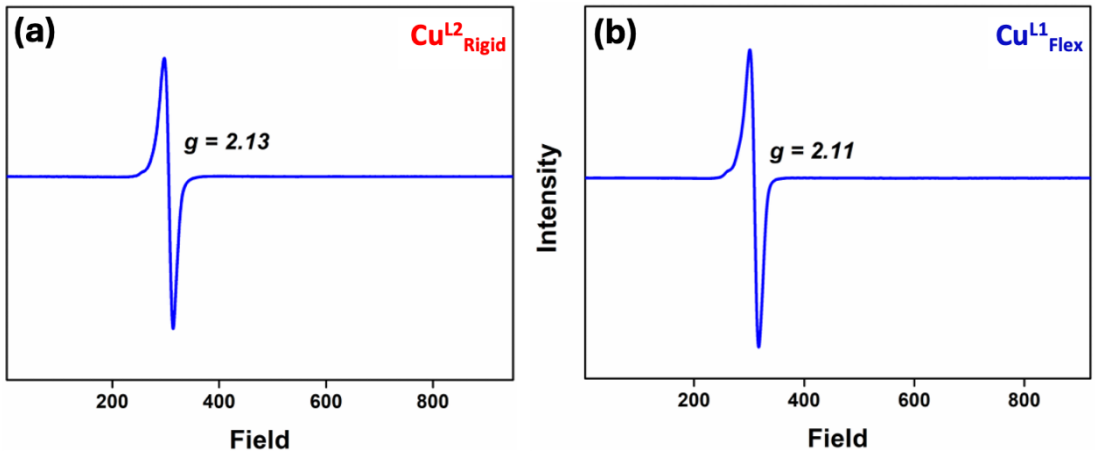

Figure S4. EPR spectra of (a) [Cu^{L2}_{Rigid}] (g = 2.13) and (b) [Cu^{L1}_{Flex}] (g = 2.11), confirming Cu(II) center

7. Electrospray Ionization Mass Spectrometry spectra (ESI-MS):

The ESI-MS spectra of the Cu (II) complexes are provided below, showing characteristic peaks corresponding to the expected molecular ion fragments.

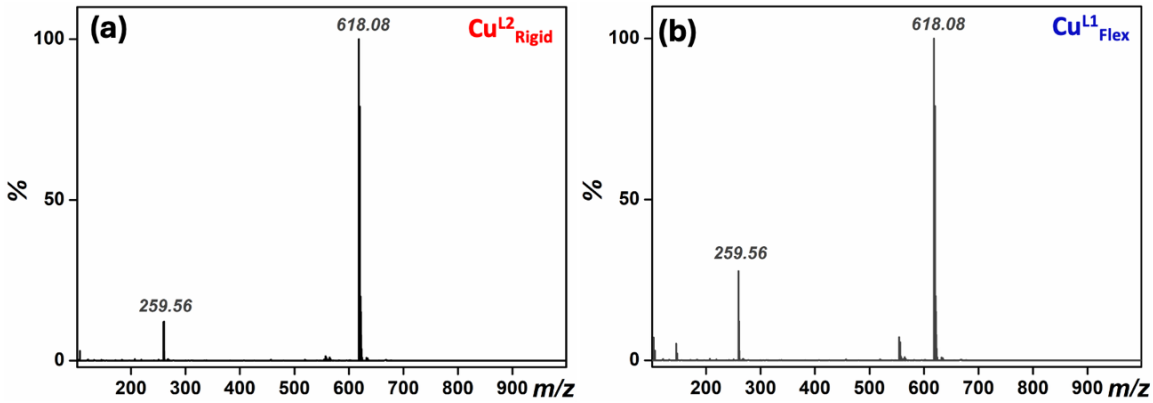

Figure S5. ESI-MS spectra of (a) [Cu^{L2}_{Rigid}] and (b) [Cu^{L1}_{Flex}] complex.

8. Crystallographic information of the two-complex molecules ([Cu^{L2}_{Rigid}] and [Cu^{L1}_{Flex}]):

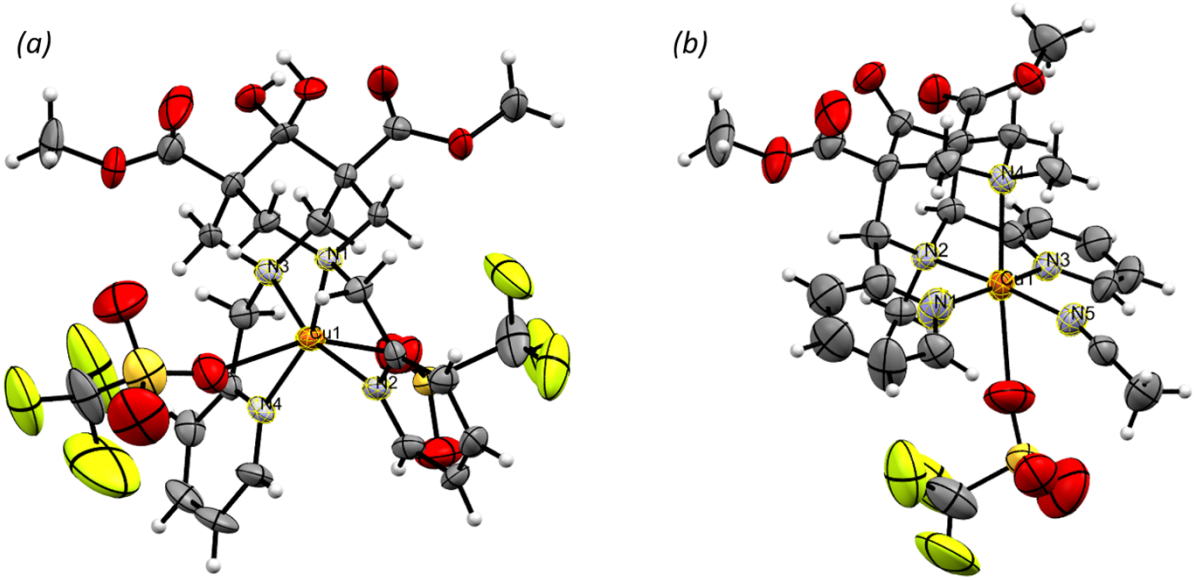

Figure S6. ORTEP images of (a) [Cu^{L1}_{Flex}] and (b) [Cu^{L2}_{Rigid}] complex (Probability=50%). Counter ions were omitted for better clarity.

Table S1. Crystallographic bond distances and bond angles for both complexes.

Complexes:	**Cu(II)_Rigid**			**Cu(II)_Flex**		
	Bonds	*r* in Å		Bonds	*r* in Å	
Axial bond	Cu1-N4	2.362	-	Cu1-N4	1.971	1.995*
Equatorial bonds	Cu1-N1	1.986	2.008*	Cu1-N1	2.016	
	Cu1-N2	2.045		Cu1-N2	1.974	
	Cu1-N3	1.995		Cu1-N3	2.022	
	Angles	θ in °		Angles	θ in °	
Trans-dihedral angles	N1-Cu1-N3	163.75		N1-Cu1-N4	160.80	
	N2-Cu1-N5	175.49		N2-Cu1-N3	162.29	
	N4-Cu1-O8	171.70		O8-Cu1-O11	158.65	
Cis-bond angles	N1-Cu1-N2	82.78		N1-Cu1-N2	85.37	
	N1-Cu1-N4	93.04		N1-Cu1-N3	88.34	
	N1-Cu1-N5	95.50		N2-Cu1-N4	105.21	
	N2-Cu1-N3	82.91		N3-Cu1-N4	85.74	
	N2-Cu1-N4	52.79				
	N3-Cu1-N4	92.96				
	N3-Cu1-N5	98.19				

9. Cyclic voltammetry of the Cu (II) complexes:

The cyclic voltammograms provided below clearly display the reversible redox peaks corresponding to the Cu^{2+}/Cu^{+} and Cu^{+}/Cu^{0} transitions for both complexes. Distinct potentials are observed for $[Cu^{L2}{}_{Rigid}]$ and $[Cu^{L1}{}_{Flex}]$, highlighting their different electronic environments and redox characteristics.

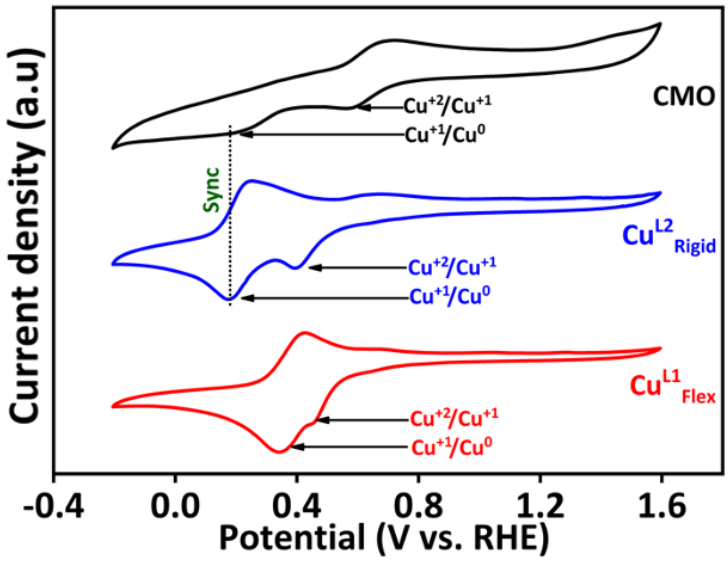

Figure S7. CV of $[Cu^{L2}{}_{Rigid}]$ (blue) and $[Cu^{L1}{}_{Flex}]$ (red) and stand-alone heterogeneous CMO catalyst (black), showing reversible Cu^{2+}/Cu^{+} and Cu^{+}/Cu^{0} couples

10. XPS analysis of the Cu (II) complexes

The XPS spectra of the Cu 2p core levels are provided below, illustrate the distinct electronic environments of the two complexes. The binding energy peaks for $[Cu^{L2}{}_{Rigid}]$ appear at lower values compared to $[Cu^{L1}{}_{Flex}]$. Specifically, the Cu $2p_{3/2}$ and Cu $2p_{1/2}$ peaks for $[Cu^{L2}{}_{Rigid}]$ exhibit negative binding energy shifts of 1.15 eV and 1.18 eV, respectively, relative to the flexible complex. This pronounced shift toward lower binding energies indicates a higher electron density at the Cu center in $[Cu^{L2}{}_{Rigid}]$. This comparatively electron-rich environment enhances the ability of $[Cu^{L2}{}_{Rigid}]$ to donate electrons during CO_2 reduction, which is highly consistent with the electrochemical data and its correspondingly higher Faradaic yield.

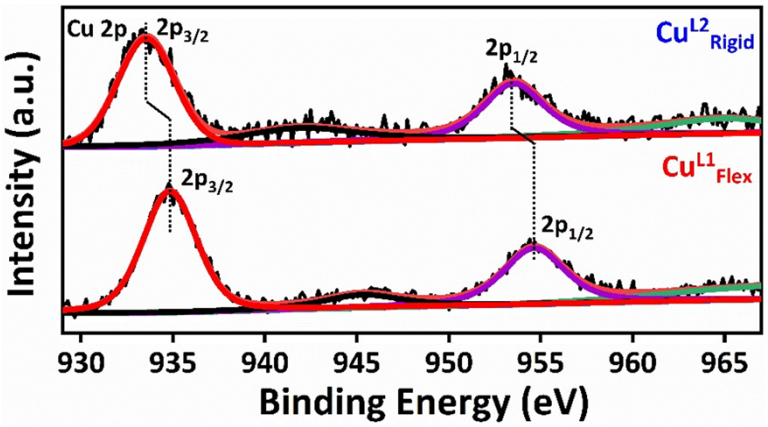

Figure S8. XPS spectra of [Cu^{L2}_{Rigid}] and [Cu^{L1}_{Flex}], showing the shift of Cu 2p binding energies.

11. Tafel analysis of the synthesized electrocatalyst:

Tafel analysis is utilized for relating the rate of an electrochemical reaction to the overpotential. The Tafel slope shows how efficiently an electrode can produce current in response to change in applied potential. The Tafel equation in an electrochemical reaction is given as,

$$\ln I = \ln I_0 + \left(\frac{\alpha n F}{RT}\right)\eta \qquad \text{(S1)}$$

Where **I** is the current, $\mathbf{I_0}$ is the exchange current (current at equilibrium potential), α is the

charge transfer coefficients for the catalytic reaction, n is the number of electrons transferred,

F is the Faraday constant (96,485 C), **R** is the ideal gas constant, **T** is the absolute temperature

and η is the overpotential.

The equation has the form of y = b + mx and will give a linear line when log I is plotted vs. η, which is the well-known 'Tafel plot'. The slope of the linear line is given as follows,

$$\text{Slope } \left(\frac{d\log I}{d\eta}\right) = \left(\frac{2.303RT}{\alpha nF}\right) \qquad \text{(S2)}$$

Thus, the equation provides a clear view that the slope of the Tafel plot is inversely related to

the charge transfer coefficient (α), which means that the lower the Tafel slope, the faster the charge transfer across the electrocatalytic interface.

12. Faradaic efficiency measurement:

The Faradaic efficiency (FE) of the products formed during CO_2 reduction was calculated using the relation:

$$FE\% = \frac{amount\ of\ product\ \times\ n\ \times F}{Q} \times 100 \quad \text{(S3)}$$

Where,

n = number of electrons involved in the formation of one product molecule

F = Faradaic constant (96485 C mol^{-1})

Q = amount of charge passed through the working electrode (C)

The amount of product formed was quantified by NMR spectroscopy using DMSO as the internal standard.

13. NMR spectra of the [Cu^{L1}_{Flex}]/CMO hybrid system and stand-alone CMO recorded at different applied potentials:

Figure S9 shows the NMR spectrum of the [Cu^{L1}_{Flex}]/CMO hybrid, while Figure S10 presents that of the stand-alone CMO. These spectra were used to derive the corresponding Faradaic efficiencies reported in the main text, enabling a direct comparison with the [Cu^{L2}_{Rigid}]/CMO system.

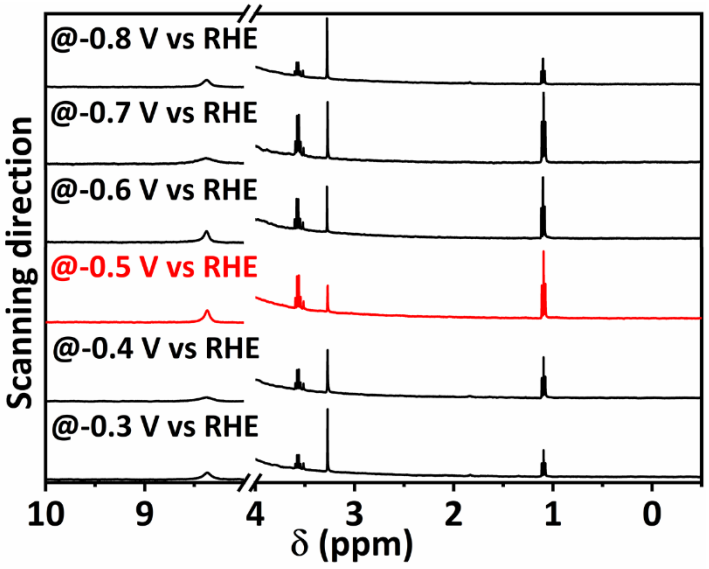

Figure S9. NMR spectra of [Cu^{L1}_{Flex}]/CMO hybrid

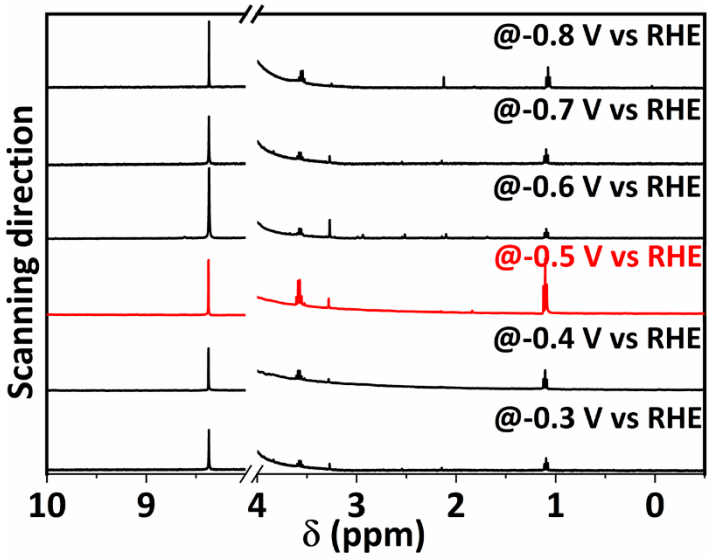

Figure S10. NMR spectra of stand-alone CMO

14. CO_2 reduction for stand-alone homogeneous catalyst:

CO_2 reduction on a glassy carbon electrode with homogeneous complexes yielded no liquid products, while gas-phase analysis confirmed CO formation. Gas chromatography showed higher CO yields for [Cu^{L2}_{Rigid}] than [Cu^{L1}_{Flex}]

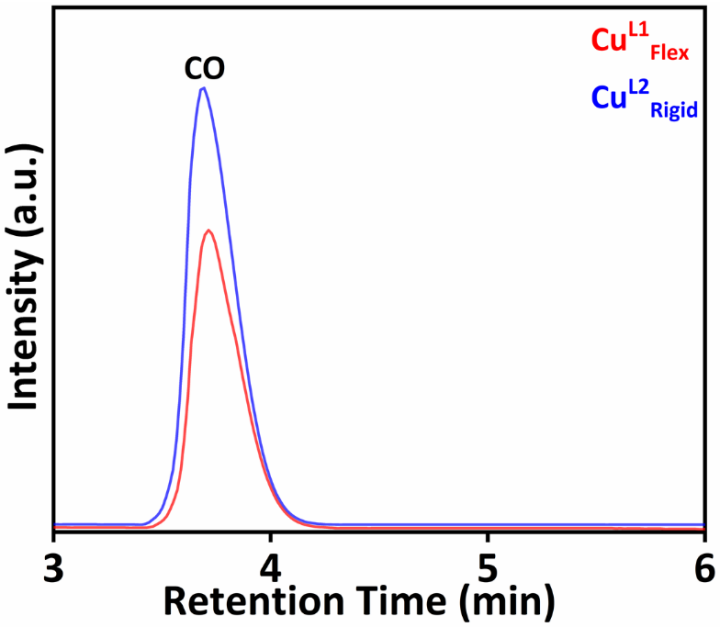

Figure S11. Gas chromatography of CO evolution in presence of stand-alone ho homogeneous catalyst.

15. Calculation of turnover frequency (TOF)

Turnover frequency (TOF) was calculated as:

$$\text{TOF} = \frac{J \,.\, A}{12 \,.\, n \,.\, F} \qquad \text{(S4)}$$

where J is the current density at a given potential, A is the surface area of the electrode (1 cm^2 for the working electrode), 12 is the number of electrons transferred in the CO_2RR for the production of ethanol, n is the number of moles of all metal ions available for the CO_2RR and F is Faraday's constant (96485 C mol^{-1}).

16. Calculation of electrochemically active surface area (ECSA):

The superior electrochemical performance is attributed to an increase in electroactive surface sites. To quantify the electrochemically active surface area (ECSA), the double-layer capacitance (C_{dl}) was evaluated from cyclic voltammograms recorded in the non-faradaic region. The CV measurements were carried out within the potential window of 0.025–0.125 V vs. RHE at a scan rate from 1mV/sec to 6mV/sec.

The double layer capacitance (C_{dl}) values were calculated from the slope of the plot between the difference in current density ($j_{anode} - j_{cathode}$) at 0.1V with respect to RHE vs scan rate (Figure S12(a-c)), where C_{dl} is equal to half of the obtained slope value.

ECSA is proportional to the C_{dl} value as follows,

$$ECSA = C_{dl}/C_s \quad (S5)$$

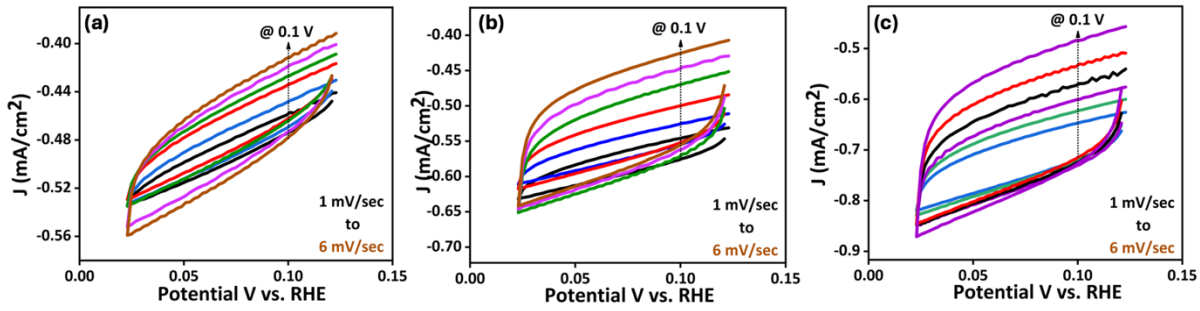

Figure S12: CVs in the non-faradaic region (0.025–0.125 V vs. RHE) at varying scan rates for C_{dl} determination.

17. ECSA normalized current density:

Normalizing the current density against the electrochemically active surface area (ECSA) is essential for a more accurate evaluation of the intrinsic catalytic activity of our materials. We have calculated the ECSA for both the standalone heterogeneous catalyst (CMO) and the hybrid systems (CMO+Cu^{L1}_{Flex} and CMO+Cu^{L2}_{Rigid}) derived from the double-layer capacitance (C_{dl}) measurements as presented in Figure 4a (main manuscript).

Subsequently, we measured the geometrical current densities at applied potentials ranging from -0.3 V to -0.8 V vs. RHE (in 0.1 V increments). This specific potential range was selected because these are the operational potentials at which we evaluated the Faradaic efficiency (FE%) to determine the optimum conditions for maximum ethanol yield. The obtained current densities were then normalized by their respective ECSA values to yield the specific activity (j_{ECSA}).

The resulting plot of j_{ECSA} versus applied potential is presented below. Notably, the ECSA-normalized data reveals the same trend observed previously: the CMO+Cu^{L2}_{Rigid} system exhibits the highest (j_{ECSA}) across all applied potentials,

validating its superior intrinsic electrocatalytic performance compared to the standalone heterogeneous and hybrid system with flexible ligand.

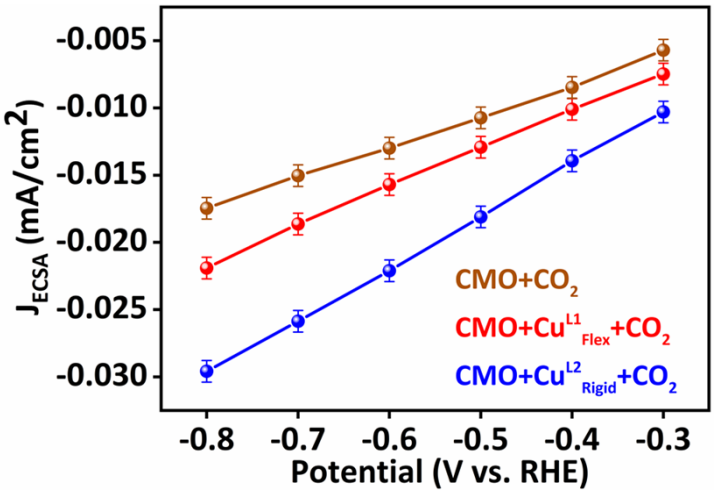

Figure S13. ECSA-normalized current density (J_{ECSA}) as a function of applied potential for the standalone CMO and hybrid CMO+Cu$^{L1}_{Flex}$, and CMO+Cu$^{L2}_{Rigid}$ electrocatalysts.

Details of ECSA Normalization and Sample Calculation:

To transparently demonstrate our methodology, the normalization of the current density was performed as follows. First, the ECSA was determined using the relationship:

$$\text{ECSA} = \frac{C_{dl}}{C_s}$$

where C_{dl} is the measured double-layer capacitance and C_s is the specific capacitance of a smooth, flat surface under identical electrolyte conditions (assumed to be ~0.040 mF/cm², The value of 0.040 mF/cm² is the widely accepted standard specific capacitance C_s for an theoretically smooth electrode surface). The normalized current density J_{ECSA} is then calculated by dividing the measured geometric current density (J_{geo}) by ECSA:

$$J_{ECSA} = \frac{J_{geo}}{ECSA}$$

Sample Calculation (CMO+Cu$^{L2}_{Rigid}$ system at an applied potential of -0.5 V vs. RHE):

- Measured geometric current density (j_{geo}): -9.2 mA/cm²
- Measured double-layer capacitance (C_{dl}): 32 mF/cm² (from Figure 4a)
- Specific capacitance (C_s): 0.040 mF/cm²

First, we calculate the ECSA:

$$\text{ECSA} = \frac{32\ mF/cm^2}{0.040\ mF/cm^2} = 800$$

Next, we calculate the ECSA normalized current density:

$$J_{ECSA} = \frac{-13.6\ mA/cm^2}{800} = \text{-0.017 mA/cm}^2$$

18. Determination of mass loading and mass activity of heterogeneous catalyst:

The mass loading of the CMO catalyst on the carbon paper substrate was determined using the weight difference method. Specifically, a standard carbon paper strip with total dimensions of 1 × 0.3 cm^2 (Length × breadth) was utilized, and the direct hydrothermal growth was restricted to a specific geometric area of 0.5 × 0.3 cm^2. The substrate was thoroughly washed, dried, and weighed before and after the deposition process using a high-precision analytical microbalance. The weight difference confirmed a total active catalyst mass loading of 0.6 mg within the deposition area.

To evaluate the intrinsic catalytic performance independently of the macroscopic electrode area, we evaluated the mass activity by normalizing the measured current by the determined catalyst mass.

At an applied potential of -0.5V vs. RHE, the CMO catalyst delivered a measured current of $3\ mA$ when Cu^{L2}_{Rigid} complex is in the homogeneous medium. Using the calculated mass loading of $0.6\ mg$, the mass activity was determined as 5 mA/mg.

$$\text{Mass Activity} = \frac{I}{m} = \frac{3\ mA}{0.6\ mg} = 5\ \text{mA/mg}$$

As our system relies on tuning the homogeneous catalyst to achieve interfacial redox synchronization-rather than stepwise modification of the heterogeneous surface-this mass activity was calculated exclusively in the presence of the Cu^{L2}_{Rigid} complex to reflect the interface's true operational state under synchronized condition.

19. Calculation of number of active sites:

The number of active sites is calculated by performing Cyclic Voltammetry (CV) in the non-Faradaic region between 0.025-0.125 *V vs. RHE* at a slow scan rate of *1mV/sec*. Performing CVs at such low scan rates allows for the optimal adsorption of

charged species on the electrode surface, thereby providing deeper and more accurate insight into double-layer formation. The CV from which the area of the C_{dl} has been calculated is presented in the figure below.

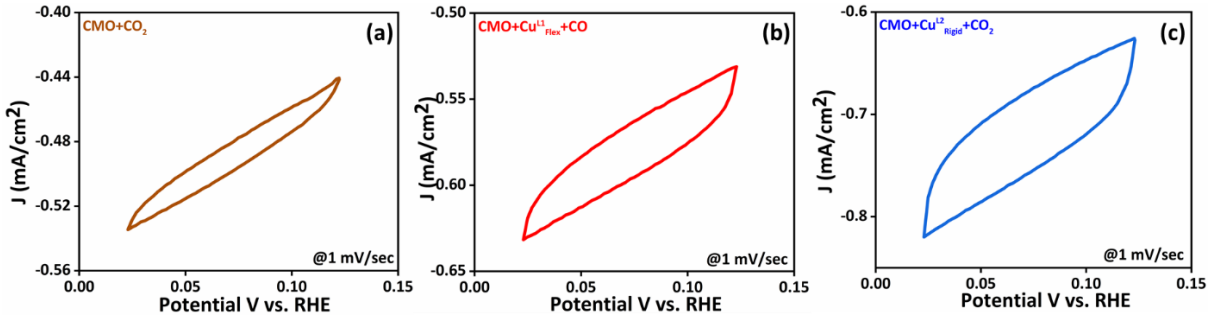

Figure S14. Cyclic voltammogram of the catalyst obtained in the non-Faradaic potential window (0.025–0.125 V vs. RHE) at a slow scan rate of 1 mV/s.

The number of active sites (τ) was calculated using the equation:

$$\tau = \frac{Area\ of\ the\ C_{dl}}{Scane\ rate\ \times\ 1.601 \times 10^{-19} C}$$

We evaluated these values for the standalone CMO heterogeneous catalyst, as well as for the hybrid systems in the presence of the $Cu^{L1}{}_{Flex}$ and $Cu^{L2}{}_{Rigid}$ complexes in the homogeneous medium. The calculated number of active sites are as follows:

- Standalone CMO catalyst: *4.25 × 10¹⁷ sites*
- CMO + $Cu^{L1}{}_{Flex}$ complex ([$Cu^{L1}{}_{Flex}$]/CMO): *5.37 × 10¹⁷ sites*
- CMO + $Cu^{L2}{}_{Rigid}$ complex ([$Cu^{L2}{}_{Rigid}$]/CMO): *6.53 × 10¹⁷ sites*

As demonstrated by these calculations, the CMO catalyst operating in the presence of the $Cu^{L2}{}_{Rigid}$ homogeneous complex possesses the highest number of accessible active sites. This significant enhancement provides further quantitative evidence for our proposed mechanism, demonstrating that the structural rigidity of the complex facilitates optimal interfacial redox synchronization and highly efficient charge transfer between the homogeneous and heterogeneous catalytic components.

20. The Distribution of Relaxation Time (DRT) methodologies:

DRT approach is a model-free method employed in the analysis of electrochemical impedance spectroscopy (EIS) data to uncover detailed physicochemical information about the system. By separating the impedance response into discrete relaxation

times, it enables the identification and interpretation of distinct electrochemical phenomena occurring within the system.

Methodologies: Open-source MATLAB script-based software (DRT Tools) was used to calculate DRT from the impedance data, and the Gaussian method was used for data discretization. The DRT plots was obtained from the EIS data using Gaussian basis function and 0.01 regularization parameter. Each peak is defined by its central position, its total area (which corresponds to its effective resistance) and its width.

The related time constant can be calculated by $t=\frac{1}{2\pi f}$. Here, *f* represents the frequency, and it is independent of the surface area and represents the intrinsic properties of each process.

Regarding parameter selection, the series resistance across the electrolyte and electrode interface possesses very small time constant, with its peak observed around 10^{-4} to 10^{-3} s.

The charge transfer at the electrode/electrolyte interface is more rapid than that of cathode materials delivering the time constant of 0.01 to 0.1 s.

The diffusion in electrodes or materials is the most sluggish process because the diffusion is only driven by the concentration gradient. The time constant for diffusion reaches more than 0.1 s to 10 s.

To calculate the contribution from each peak we have to follow the steps given below:

1. We have to find out the total area by summing up all the area of peak, where peak area represents the impedance of the corresponding process.

2. Next step is to find out the total resistance (uncompensated and charge transfer resistances are denoted as R_u and R_{ct}, respectively) from the fitted EIS Nyquist plot.

21. Post-electrochemical characterization of the catalyst:

21.1 FESEM characterization of the heterogeneous catalyst post-electrocatalysis:

Post-electrocatalysis FESEM analysis (shown below) confirms that the hexagonal sheet-like morphology of the catalyst remains well preserved after electrochemical operation, highlighting its excellent structural robustness and mechanical integrity under reaction conditions.

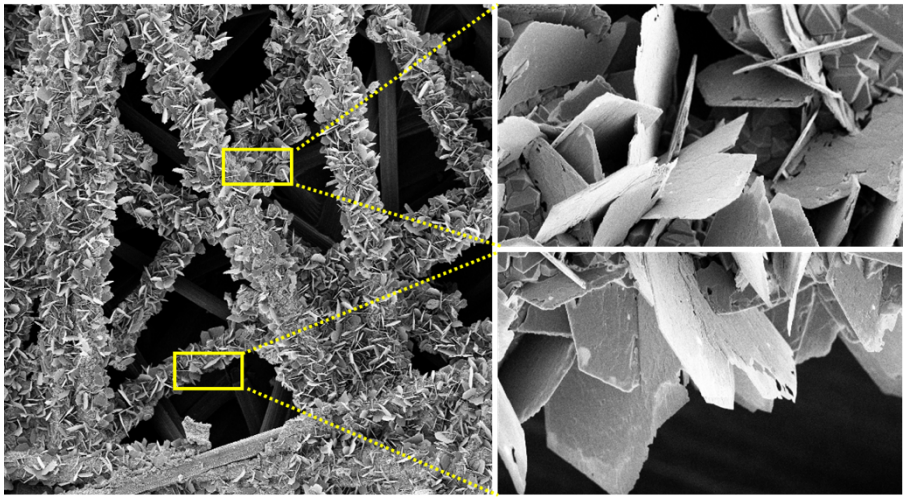

Figure S15: FESEM image of the catalyst after electrocatalysis showing intact hexagonal sheet morphology.

21.2 Post-electrocatalysis XRD characterization of the heterogeneous catalyst:

To evaluate the overall structural integrity of the heterogeneous catalyst, XRD analysis before and after electrocatalysis was performed. These XRD measurements were taken over a carbon paper substrate, as the catalyst deposition had been done *in situ*. The resulting diffraction patterns showed no new peaks, this confirms that the catalyst maintained its original phase, underscoring the robust structural stability of the heterogeneous catalyst under the applied electrochemical conditions.

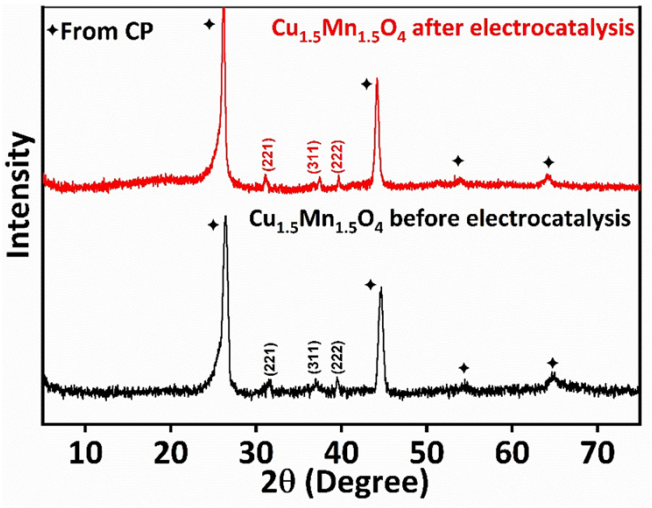

Figure S16: XRD pattern of the heterogeneous catalyst recorded after electrocatalysis.

21.3 UV–Vis Characterization of the Homogeneous Catalyst after Electrocatalysis:

To evaluate the stability of the homogeneous molecular catalysts during electrocatalytic CO_2 reduction, post-electrolysis UV–Vis spectroscopy was performed for both complexes (Cu^{L1}_{Flex} and Cu^{L2}_{Rigid}, Figure S15). The spectra reveal that the characteristic absorption features remain unchanged after electrolysis, as evidenced by comparison with the pre-electrolysis spectrum shown in Figure S3, confirming that the molecular frameworks of the catalysts are preserved under the applied reaction conditions.

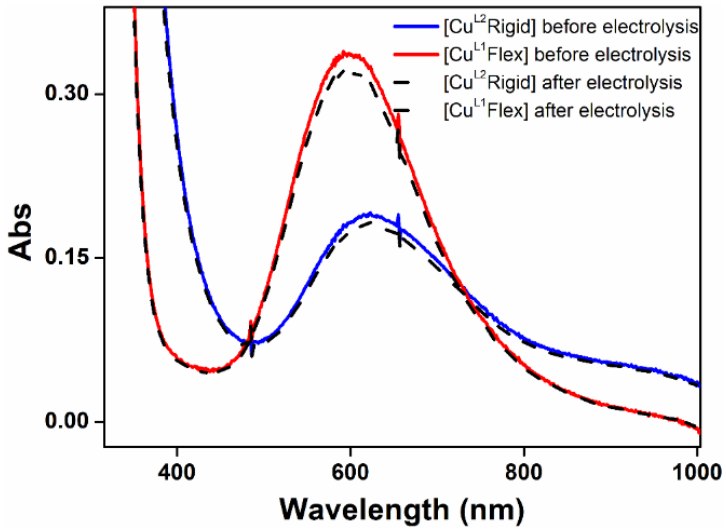

Figure S17: UV–Vis spectra of Cu^{L1}_{Flex} and Cu^{L2}_{Rigid} recorded before and after electrocatalysis.

22. Synthesis Protocol for CuO and its Characterization:

Synthesis Protocol: 1 mmol of copper acetate ($Cu(CH_3COO)_2$) and 6 mmol of sodium acetate (CH_3COONa) were dissolved in 40 mL of deionized water to form a homogeneous solution. This solution was then transferred into a Teflon-lined stainless-steel autoclave and heated at 150 °C for 12 hours. After the reaction, the resulting compound was collected, thoroughly rinsed with ethanol and deionized water, and dried under vacuum at 60 °C followed by calcination in air at 450 °C for 4 hours with a heating rate of 5 °C/min to obtain the final CuO phase.

PXRD Analysis and Phase Purity: From the PXRD analysis it has been observed that peaks at 2θ values 32.48°, 35.47°, 38.62°, 48.64°, 53.23°, 58.23°, 61.63°, 66.13°, 68.20°, 72.34° and 75.0° are corresponding to (110), (002), (111), (-202), (020), (202), (-113), (-311), (220), (311) and (004) planes of CuO respectively ((ICSD No. 00-005-0661).

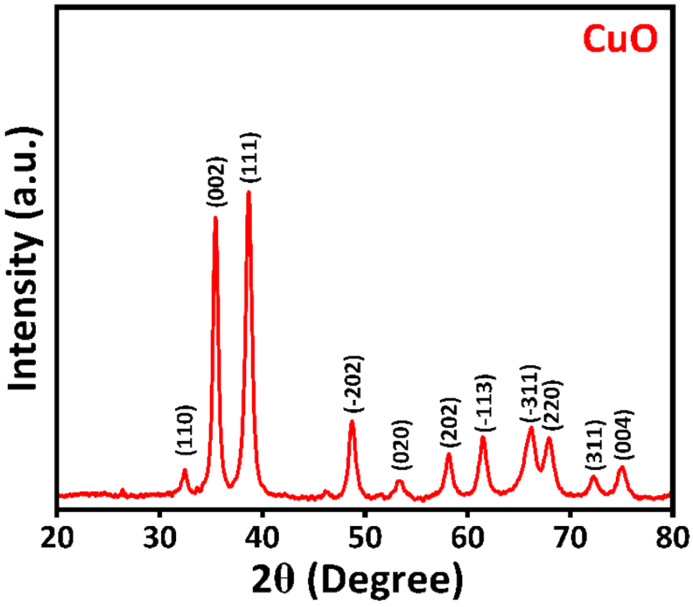

Figure S18: Powder X-ray diffraction (PXRD) pattern of the as-synthesized CuO. The diffraction peaks are indexed to the pure monoclinic phase of CuO (ICSD No. 00-005-0661)

23. Computational Details:

All density functional theory (DFT) calculations were executed with the Vienna ab initio Simulation Package (VASP) [5,6] where the electron-ion interactions were described using the projector augmented wave (PAW) pseudopotentials, and the Perdew-Burke-Ernzerhof (PBE) functional within the generalized gradient approximation (GGA) was employed to account for exchange-correlation effects [7,8]. The Grimme D3 dispersion correction was applied to include long-range van der Waals (vdW) interactions (DFT + D3) [9]. The plane-wave energy cut-off was set at 400 eV. A 25 Å vacuum layer was employed as the substrate model along the z-axis. A 3×3×1 Monkhorst-Pack *k*-point mesh was employed for Brillouin zone sampling [10]. The optimal hydrogen adsorption configuration was determined using potential energy curves (PECs) with different orientations of the gas molecule (parallel, perpendicular, and tilted), as shown in Figure S16. The adsorption energy can be defined as [11]

$$E_{ads} = E_{H_2 + System} - \left(E_{System} + E_{H_2}\right) \qquad (S6)$$

Here, E_{ads} , $E_{H_2+System}$, E_{System} and E_{H_2} represents the total adsorption energy, the energy of the H_2 adsorbed system, the system energy, and the energy of hydrogen. Further, the Gibbs free energy of the hydrogen evolution reaction (HER) can be calculated as

$$G_{H*} = \triangle E_{H*} + \triangle E_{ZPE} - T \triangle S \qquad (S7)$$

In Eqn. (2), G_{H*}, E_{H*}, E_{ZPE}, and $\triangle S$ represents Gibbs free energy, H-adsorption energy, zero-point energy, entropy correction, T at 298 K. [11,12]

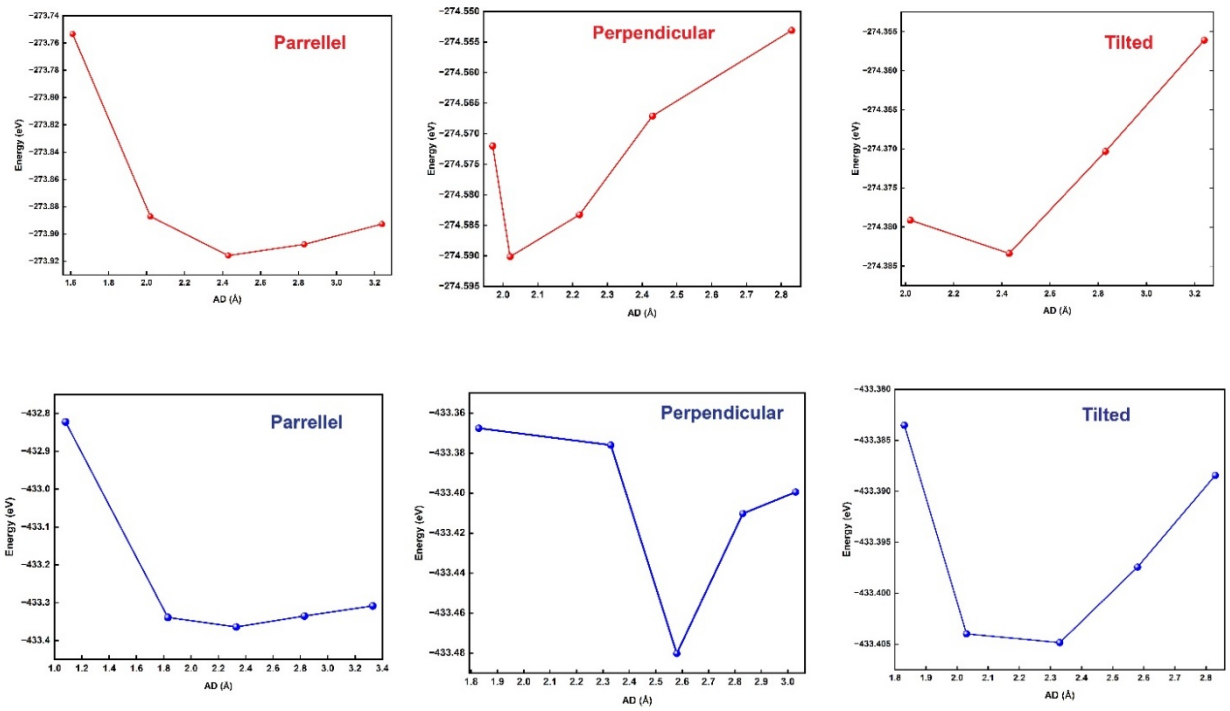

Figure S19: Potential energy curves (PECs) for CuO (Red) and $Cu_{1.5}Mn_{1.5}O_4$ (Blue) with different orientations of the H_2-molecule.

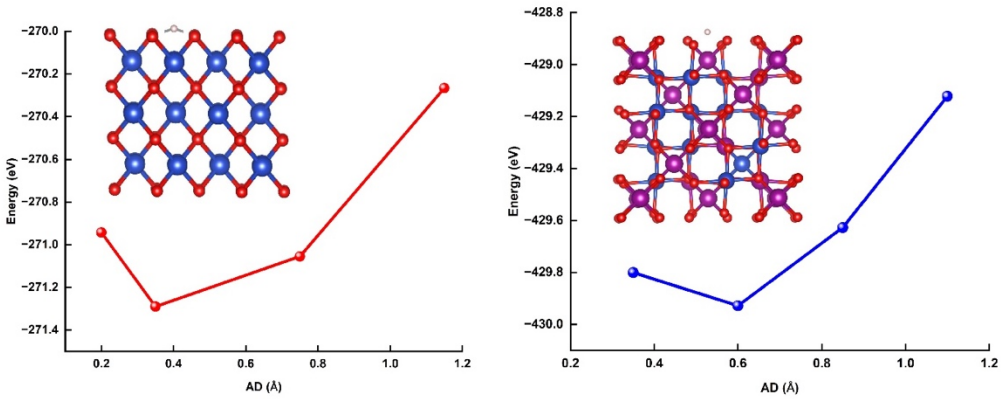

Figure S20: Potential energy curves (PECs) for CuO (Red) and $Cu_{1.5}Mn_{1.5}O_4$ (Blue) after H-adsorption with most of the preferable structures.

24. Comparison Table:

summarizes representative recent studies on Cu-based catalytic systems for CO_2 electroreduction to ethanol, including heterogeneous, and semi-hybrid approaches. Key performance metrics such as catalytic system, electrolyte, and Faradaic efficiency toward ethanol are compared to provide a clear benchmarking framework. This comparison highlights the relative position and effectiveness of our hybrid Cu-based catalyst within the current state-of-the-art.

Table S2: Comparative overview of recently reported Cu-based catalysts for electrochemical CO_2 reduction to ethanol

Category	Catalyst System	Electrolyte Used	Faradaic Efficiency for Ethanol (%)	Reference
Heterogeneous	nitrene-functionalized Cu catalyst	1M KOH	45%	**13**
Heterogeneous	Cobalt and copper atoms anchored to electrically conductive nitrogen-doped carbon	0.1M $KHCO_3$	70%	**14**
Heterogeneous	CuAg@NTA	0.25M $KHCO_3$	70%	**15**
Heterogeneous	$Cu_2(OH)_3F$	1M KOH+1M KCl	50%	**16**
Heterogeneous	Nanograin-Boundary-Rich Mixed Cu(I)/Cu(0) Sites	Saturated $KHCO_3$	53.5%	**17**
Heterogeneous	Pd-incorporated cu alloy	0.1M $KHCO_3$	57%	**18**
Heterogeneous	CoPc/$Cu_{2-x}Se$ tandem electrode	0.5M $KHCO_3$	59%	**19**
Heterogeneous	Nanostructured of Cu_2O catalysts	0.5M $KHCO_3$	52.6%	**20**
Semi-hybrid System (Direct Integration of Molecular and Heterogeneous Catalysts)	Fe-TPP complex over 3D nickel heterogeneous catalyst	0.5M $KHCO_3$	68±3.2%	**21**
Hybrid System	**Cu1.5Mn1.5O4/[Cu^{L2}_{Rigid}]**	**1M Phosphate buffer**	**68%**	**(Present Work)**

25. References

1. N. Kalita, J. K. Satpathy, R. Yadav, C. Sastri and M. Qureshi, *Chem. Mater.* 2025, **37**, 2026.

2. P. Comba, C. L. de Laorden and H. Pritzkow, *Helv. Chim. Acta* 2005, **88**, 647.

3. G. Mukherjee, J. K. Satpathy, U. K. Bagha, M. Q. E. Mubarak, C. V. Sastri and S. P. de Visser, *ACS Catal.* 2021, **11**, 9761–9797.

4. G. Mukherjee,and C. V. Sastri, *Isr. J. Chem.* 2020, **60**, 1032.

5. G. Kresse and J. Furthmüller, *Comput. Mater. Sci.* 1996, **6**, 15.

6. G. Kresse and J. Furthmüller, *Phys. Rev. B.* 1996, **54**, 11169.

7. J.P. Perdew, K. Burke and M. Ernzerhof, *Phys. Rev. Lett.* 1996, **77**, 3865.

8. P.E. Blöchl, *Phys. Rev. B.* 1994, **50**, 17953.

9. S. Grimme, J. Antony, S. Ehrlich and H. Krieg, *J. Chem. Phys.* 2010, **132**, 154104.

10. H.J. Monkhorst and J.D. Pack, *Phys. Rev. B.* 1976, **13**, 5188.

11. H. Yang, X. Xia, S. An, M. Huang, H. Ma, F. Ye, C. Peng and C. Xu, *RSC Adv.* 2025, **15**, 7682.

12. U. Nath and M. Sarma, *J. Phys. Chem. C.* 2025, **129**, 13939.

13. Z. Liu, L. Song, X. Lv, M. Liu, Q. Wen, L. Qian, H. Wang, M. Wang, Q. Han and G. Zheng, *J. Am. Chem. Soc.*, 2024, **146**, 14260.

14. S. A. Chala, R. Liu, E. O. Oseghe, S. T. Clausing, C. Kampf, J. Bansmann, A. H. Clark, Y. Zhou, I. Lieberwirth, J. Biskupek, U. Kaiser and C. Streb, *ACS Catal.*, 2024, **14**, 15553.

15. H. Liu, Y. Yu, Y. Bai, et al., *Nat. Commun.*, 2025, **16,** 6186.

16. Y. Da, J. Chen, L. Fan, R. Jiang, Y. Xiao, M. Wang, G. Chen, Z. Tian, H. Zhang, H. Jin, X. Chen, C. Ji, S. Xi, Y. Lum, L. Wang, T. Zhu, J. Zhang and W. Chen, *Angew. Chem., Int. Ed.*, 2025, **64**, e202506867.

17. T. Zhang, S. Xu, D. L. Chen, T. Luo, J. Zhou, L. Kong, J. J. Feng, J. Q. Lu, X. Weng, A. J. Wang, Z. Li, Y. Su and F. Yang, *Angew. Chem., Int. Ed.*, 2024, **63**, e202407748.

18. H. Huang, T. H. Tsai, Z. Y. Huang, M. K. Tsai, T. C. Chou, *Chem. Eng. J.*, 2025, **523**, 168675.

19. J.H. Wang, J. Cheng, H.K. Lv, K. Zhang, L.W. Ding, R.H. Jin, Y. Xu, Y.X. Mao *Chem. Eng. J.*, 2025, **509**, 161316.

20. F. Yang, T. Yang, J. Li, P. Li, Q. Zhang, H. Lin and L. Wu, *J. Catal.*, 2024, **432**, 115458.

21. M. Abdinejad, A. Farzi, R. Mo¨ller-Gulland, F. Mulder, C. Liu, J. Shao, J. Biemolt, M. Robert, A. Seifitokaldani and T. Burdyny, *Nat. Catal.*, 2024, **7**, 1109